Biotribology 20 (2019) 100108

Contents lists available at ScienceDirect

Biotribology

journal homepage: www.elsevier.com/locate/biotri

Diffraction gratings alter the surface friction of iridescent beetle cuticle against fibrous surfaces

Lihua Wei[a], Kristen E. Reiter[b], Thomas McElrath[b,c], Marianne Alleyne[b], Alison C. Dunn[a,*]

[a] Department of Mechanical Science & Engineering, University of Illinois at Urbana-Champaign, USA
[b] Department of Entomology, University of Illinois at Urbana-Champaign, USA
[c] Illinois Natural History Survey, University of Illinois at Urbana-Champaign, USA

ARTICLE INFO

Keywords:
Microstructured surfaces
Wet adhesion
Friction modeling

ABSTRACT

Background: Iridescence caused by physical diffraction gratings is observed on various species of beetles. Because the diffraction arises from microsculpturing on the exterior cuticle, we hypothesize that in addition to optical properties, these surface features also modify the surface friction and wettability when sliding against a nature-mimicking countersurface.

Methods: The surface friction differences between five contrasting pairs of closely related species (10 species total from 3 different beetle families) sliding against a fibrous countersurface were measured using microtribometry in both wet and dry configurations. Goniometry and cuticle geometry were used as inputs to a friction model. Finally, scanning electron microscopy was used to characterize the surface features for contextualizing the friction and fit to the model.

Results: Coefficients of friction for all species increased by a factor of at least two in the wet configuration versus the dry configuration. No consistent increase or decrease in friction or wettability was due to the diffraction gratings, but trends were consistent within beetle families: in both pairs of scarabs, the high-aspect protrusions on the iridescent beetles decreased wettability and modified friction. Results were less distinct in the carabids and staphylinids.

Discussion: The morphology of the beetle surfaces rather than the presence of a physical diffraction grating determines their wettability and friction behavior when sliding against a wet, fibrous surface. The roughness and orientation of features controls the area in contact, and dynamic changes in the contact give rise to friction.

1. Introduction

Iridescent appearance is ubiquitous in the insect world, and can be found on the hard, exterior cuticle of the order Coleoptera, or beetles. The anatomy and mechanisms which diffract broad-spectrum light to give the iridescent appearance are varied, from physical diffraction gratings to multilayer reflectors to photonic crystals [1]. Though diffraction gratings were the first to be described [2], they are the least understood with regard to their purpose and function. Diffraction gratings on a body surface originate in micro- or nanoscale arrays of parallel ridges or slits that disperse incident white light into its constituent wavelengths, giving the appearance of a rainbow; the iridescence can shift and move on a contoured surface as the light source moves because the maximum reflectance of each wavelength relies on the angle of incidence [3]. They are typically found on contoured surfaces of elytra (wing covers) or tergites (dorsal, abdominal segments) of beetles across multiple families.

Because iridescence is only visible in direct sunlight and has a limited ability to be detected by other beetles [1,4–6], its function may not be solely optical, but could be physical, as beetles maneuver across varied terrain which contacts the exterior of their body segments [1]. Previous studies on the functionality of diffraction gratings on beetles, notably on the elytra, focused on their optical properties. Hinton & Gibbs studied diffraction gratings on some carabids (Coleoptera: Carabidae) and water beetles (Coleoptera: Gyrinidae) and concluded that an advantage of possessing diffraction gratings comes from the rapid changes in color and reflectance of the reflected spectrum depending on the angle of view, which could both provide warning coloration and distraction that makes it difficult for predators to estimate a beetle's size and distance [7,8]. However, for the beetle families that dwell on land and move by burrowing under soil and vegetation (Fig. 1), they are unlikely to make use of the optical properties of diffraction gratings on

* Corresponding author at: Univ. of Illinois at Urbana-Champaign, c/o MechSE, 1206 W Green St MC244, Urbana, IL 61801, USA.
E-mail address: acd@illinois.edu (A.C. Dunn).

https://doi.org/10.1016/j.biotri.2019.100108
Received 5 August 2019; Received in revised form 13 September 2019; Accepted 27 September 2019
Available online 21 October 2019
2352-5738/

Fig. 1. Many beetles move by scurrying under leaf litter and burrowing through substrates present in their environment, including particulates such as soil, as well as fibrous matters such as leaf litter and decaying wood. As beetles burrow, their dorsal cuticle touches the substrate, resulting in dry or liquid-mediated contacts between their dorsal cuticle and natural surfaces. Under such conditions the friction force the beetles experience as their cuticle slides against natural surfaces is influenced by surface chemistry and roughness of their cuticular surfaces. Since diffraction gratings are usually found on outer surfaces of elytra or tergites, which are surfaces that directly interact with the environment, we hypothesized that the presence of diffraction gratings affects tribological performance of the cuticle on elytra or tergites. Figure by Olivia Boyd.

body surfaces. Further, more recent studies have found correlations between the possession of diffraction gratings and burrowing behaviors [1,4–6]. Many beetle species with burrowing behavior possess blazed gratings that might or might not cause diffraction, and some species with diffraction gratings tend to live in leaf litter, soil, decaying matter, etc. [4–6]. The studies on carabid beetles also showed that species in damp microhabitats have diffraction gratings, but not those in dry microhabitats. All of these studies suggest that the evolution of diffraction gratings on beetles is related to their burrowing behavior, especially in wet habitats. *Thus, we hypothesize that these diffraction gratings on beetle surfaces also serve a physical function, specifically modification of tribological properties and wettability*. This modification is advantageous as it would help mediate the beetle's sliding through its environment during burrowing. Specifically, the microfeatures acting as a diffraction grating on a beetle elytron or tergite also provide regular patterns of asperities on the surface, which control surface roughness and real contact area, leading to modification of the tribological properties and wettability of the body surface.

The extent to which these diffraction gratings modify interactions with the environment requires a comparison with baseline species that do not have the physical diffraction gratings. While many beetles exhibit iridescence, some of their closely related species within the same genus or family do not. The closely related pairs of species studied here allow for apt contrast in properties. Since this manuscript only addresses diffraction gratings, and no other iridescence mechanisms, the term “iridescent” is used to describe species with diffraction gratings, and the term “non-iridescent” is used to describe species without diffraction gratings.

In this work, we tested the hypothesis that physical diffraction gratings modify the friction and wettability of beetle cuticle by directly measuring the surface friction of elytral or abdominal surfaces in five pairs of closely related species. We then assembled a model of friction for the case of beetle cuticle sliding against a fibrous surface in the presence of a water film. Measurements of wettability and geometry are featured in the model, and are compared to the experimental results. Finally, the friction and wettability are contextualized by the specific microsculptures, or surface features, present on each samples surface, as imaged by scanning electron microscopy (SEM). This work provides the first multi-technique assessment and modeling of the cuticle slip of phylogenetically-related iridescent species pairs, with implications for understanding the role of multifunctional exoskeletons in burrowing insects.

2. Materials and Experimental Methods

2.1. Sample Selection and Preparation

Beetle specimens studied were chosen from a database of beetles with diffraction gratings [9], which was then compared to the holdings of the Illinois Natural History Survey Insect Collection located at the University of Illinois at Urbana-Champaign (Urbana, IL). When an iridescent species was found within the collection with enough samples available ($n = 6$), its nearest non-iridescent relatives, based on published phylogenetic studies or revisions [10–12], were then also checked for availability ($n = 6$). From these criteria, we were able to select a number of contrasting pairs of closely related species within different parts of the Coleoptera phylogeny, and with different kinds of diffraction grating producing structures (Supplementary Table S1).

Multiple individuals for every species were pulled from INHS Insect Collection for the experiments. Initially fixed on points or on insect pins, beetles were rehydrated and removed from the insect pin or point. Multiple individuals per species were checked for the presence or absence of diffraction gratings by exposing the beetles to direct light and looking for full spectral (“rainbow” like) iridescence, which is due to the presence of diffraction gratings rather than other iridescence mechanisms. The carabid and scarabaeid beetles (Coleoptera: Scarabaeidae) exhibited diffraction gratings on their hardened forewings (elytra), whereas staphylinid beetles (Coleoptera: Staphylinidae), which have very short forewings, have full spectral iridescent dorsal abdominal segments (tergites). Three individuals per species were prepared for tribological experiments and goniometry measurements. Beetles were cleaned by a Branson 3510R-DTH Ultrasonic Cleaner (Danbury, CT), and moisture was removed by drying them in lab air for > 24 h. The elytra or tergites were then removed from the whole beetle using micro-dissection tools; the remaining beetle body parts were not used for the experiments and measurements presented herein, and were returned to the collection as vouchers.

2.2. Scanning Electron Microscopy

Scanning electron microscopy (SEM) was conducted to characterize the external cuticle microstructure. For each species, one whole beetle sample was dedicated for SEM. Additional elytra of *Serica* spp. and *Selenophorus* spp. pairs were used to take cross-sectional images by freeze fracturing technique [13], in which elytra were dissected and immersed in liquid nitrogen, then fractured further using a scalpel. Samples were mounted on aluminum stubs using double-sided carbon tape (Structure Probe, West Chester, PA) and sputter-coated with 7 nm Au/Pd (Denton Desk II TSC, Denton Vacuum, Moorestown, NJ) at the Microscopy Suite, Imaging Technology Group, Beckman Institute for Advanced Science and Technology, University of Illinois at Urbana-Champaign (Urbana, IL). Under high vacuum, a 5 kV electron beam focused on the dorsal surfaces of elytra (FEI Quanta FEG 450 ESEM, Microscopy Suite, at UIUC's Beckman Institute). Images of high resolution were taken at 1000×, 5000×, 10,000× and 30,000× magnification. The cross-sectional images were taken at a small tilt angle at locations away from the fractured surface. Characteristic lengths, widths and sizes of micro-sculptures on the elytral surfaces were measured by image processing software based on the SEM scale bars (ImageJ [14]).

2.3. Tribological Experiments

2.3.1. Instrumentation and Testing Conditions

A custom pin-on-disk tribometer setup was used to measure friction forces and normal forces, whose ratio defines a coefficient of friction, μ

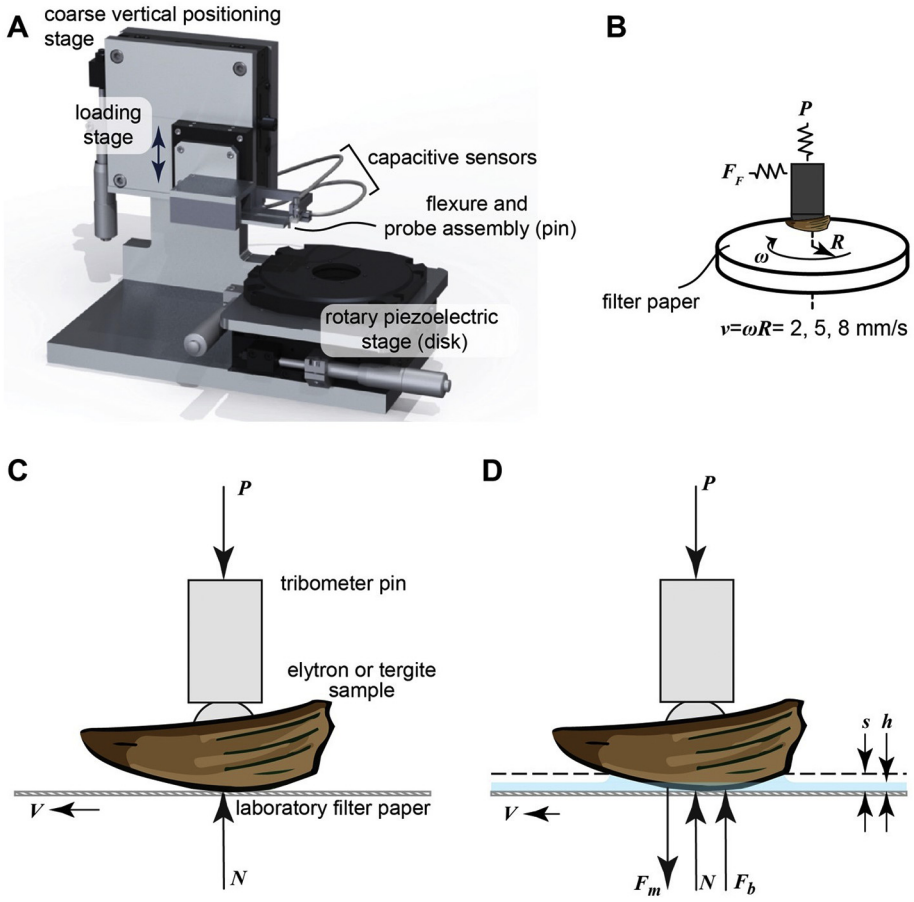

Fig. 2. (A) Pin-on-disk microtribometer setup used in this study. (B) Schematics of experimental parameters for tribometer tests under dry and wet condition. The speed $\boldsymbol{V}$ is prescribed through the rotational speed $\boldsymbol{\omega}$ and the radius $\boldsymbol{R}$. The normal capacitive sensor measures the force applied by the flexure, which opposes the sum of all contact forces in normal direction. This force is external to the contacting system, and thus is denoted externally applied load ($\boldsymbol{P}$). The lateral sensor measures the resulting friction force $\boldsymbol{F_F}$. (C) and (D) Schematics of side view and free-body diagrams of the elytron/tergite in contact with filter paper, under (C) dry condition where the externally applied load $\boldsymbol{P}$ equals to the contact load $\boldsymbol{N}$, and (D) wet condition, where a meniscus is present around the periphery of contact (height $\boldsymbol{s}$) and the elytron/tergite is partially immersed in water (water height $\boldsymbol{h}$). The buoyancy force $\boldsymbol{F_b}$ lifts the sample, and the meniscus for $\boldsymbol{F_m}$ lowers it. The externally applied load $\boldsymbol{P}$ thus equals to the sum of contact load $\boldsymbol{N}$, meniscus force $\boldsymbol{F_m}$ and buoyancy force $\boldsymbol{F_b}$. (Eq. (3)). (All gravitational effects are neglected due to zeroing of normal load measurement prior to the contact.)

(Fig. 2A) [15]. It utilizes a 500-μm stroke piezoelectric stage of 0.5 nm resolution and 0.1 N/μm stiffness to precisely lower the instrumented head to apply a normal force between a probe and substrate (P-625.1CD PIHera Piezo Linear Precision Positioner, Physik Instrumente GmbH, Karlsruhe, Germany). The probe tip experienced micro-motions accommodated by a 4-bar flexure of normal stiffness 49.136 N/m and lateral stiffness 66.157 N/m, and two capacitive probes with sensitivity of 0.2 V/μm and RMS resolution of 3.66 nm measured the deflections of the tip (C6-E, Lion Precision, Oakdale, MN). The probe geometry on which specimens were mounted was a 1-mm diameter steel ball bearing affixed to a 2-mm diameter standoff rod, attached to the flexure with cyanoacrylate adhesive (Loctite Super Glue ULTRA Gel Control, Henkel Corporation, Rocky Hill, CT). The elytra or tergites were first dissected from the individual, then sectioned using scissors and adhered on the interior side to the sphere, presenting the dorsal surface toward sliding countersurface (Fig. 2B).

Sliding was prescribed through rotation of an aluminum plate mounted on a rotary piezoelectric stage of 108-mm diameter, maximum velocity of 4 π rad/s and resolution of 34 μrad, and it provided unidirectional, constant-speed rotation (M-660.55 PILine Rotation Stage, Physik Instrumente GmbH, Karlsruhe, Germany). Samples were oriented such that the sliding always proceeded from the anterior to posterior of the elytra or tergites, aligning with setae (hair) direction, when present. Prior to the contact between the probe and countersurface, the normal and frictional force readings were zeroed to eliminate any voltage offset. As a result, any normal load readings during the experiments were free of any gravitational effects. The externally applied load by the flexure on the specimen before the initiation of sliding was to a nominal value of $\boldsymbol{P}$ = 1.0 mN, which is of the same order as the mass of a beetle, ~25 mg [16]. Roughness and runout on the order of single micrometers caused the instantaneous normal force applied to vary between 0 and 4 mN, but forces were continuously recorded at 200 Hz, ensuring accuracy of measurements.

2.3.2. Countersurfaces

The surfaces mated against the cuticle tissues were selected to both mimic fibrous plant surfaces and also provide a consistent texture to ensure identical conditions in each experiment. Laboratory filter paper manufactured from plant fibers with a thickness of 180 μm was used in all experiments (Whatman Grade 1 laboratory filter paper, GE Healthcare UK Limited, Buckinghamshire, UK). Filter paper was cut into 50 mm × 50 mm squares and adhered to a glass slide of the same dimensions, which was then adhered to the aluminum away from the probe contact region, using double-sided tape. For every individual, the sample surface slid against the counter-surface at angular speeds of 0.04 π, 0.10 π, and 0.16 π rad/s, with three trials per sliding speed. The sliding track had a radius of 16.00 mm, corresponding to linear sliding speeds of 2, 5, and 8 mm/s (Fig. 2B). These are similar to maximum speeds of beetle movement [17,18]. For each trial, the sliding distance was a total of 500 mm. The frequency of data acquisition was 200 Hz, and at each time the externally applied load $\boldsymbol{P}$ and friction force $\boldsymbol{F_F}$ were recorded (SCB-68 DAQ, National Instruments, Austin TX). For analysis, the forces were converted from normal and lateral deflections of the flexure tip through the known stiffnesses of the flexure.

Sliding experiments on all species were performed against both a dry filter paper and wet filter paper (Fig. 2C and D). Before starting an experiment with wet paper, water was sprayed four times from a commercial spray bottle, depositing ~3 g of water onto the paper, which resulted in a hydrated paper plus a water film of thickness ~ 1.25 mm. The average roughness of these filter papers under dry and wet conditions were $\boldsymbol{S_{a,dry}}$ = 6.83 ± 0.20 μm and $\boldsymbol{S_{a,wet}}$ = 8.91 ± 0.24 μm (Keyence VK-X1000, Keyence Corporation,

Itasca IL USA) [19]. Water was reapplied by spraying once every 10 min to account for evaporation during the sliding friction experiments. The tribometer setup and experimental parameters were the same as the dry paper sliding friction experiments. The forces were zeroed when the surfaces were close, but not touching, so that the forces due to water contact were measured.

2.3.3. Data Processing

The data points of time and force recorded during the sliding tests were saved in text format and processed through a script (MatLab, Mathworks Inc., Natick MA USA). First, all data from the initial and final 10 s of each experiment was removed to avoid analyzing homing protocols of the piezoelectric stage. In addition for the experiments in the dry condition, any data indicating a negative applied load were removed, as those points indicate a temporary non-contacting condition between the sample and countersurface. Under the wet condition, normal loads below zero did not necessarily mean a non-contacting condition due to the meniscus force, and as such were not omitted (see Section 3). Boxcar averaging was done over sections of 9 serial points. This resulted in sets of data of approximately ~3000 points of forces for each experiment. Given the definition of coefficient of sliding friction as the ratio of friction force to contact load $\boldsymbol{\mu = F_F/N}$, we plot $\boldsymbol{F_F}$ on the abscissa and $\boldsymbol{P}$ on the ordinate such that a least-squares regression fit to a line (Eq. (1)) results in two parameters: the slope μ defines the friction coefficient, and the y-axis intercept $\boldsymbol{F_{INT}}$. The intercept values were analyzed and interpreted in later sections.

$$F_F = \mu P + F_{INT} \tag{1}$$

2.4. Geometrical Description and Measurement of Surfaces

Beetle elytra and tergites are contoured structures with spatially-varying effective curvatures. Considering a top view and side view of a typical *Serica sericea* individual (Fig. 3A and B), the exterior anatomy in each projected view can be generally described as an ellipse. In addition, the curvature from a front view (not shown) can be described as a circle. Therefore, we modeled the beetle body as a spheroid (Fig. 3C), which is a revolution of an elliptical cross-section; it has a circular cross-section in one perspective (our front view) and elliptical cross-sections in the two other dimensions. The dimension of a spheroid can be described using only two principal radii ($\boldsymbol{R_x}$ and $\boldsymbol{R_y = R_z}$), where $\boldsymbol{R_x}$ is the principal longitudinal radius to the beetle body and $\boldsymbol{R_y}$ is the transverse radius. Since an elytron or tergite is a portion of the dorsal surface of a whole beetle, we described it as a surface section of a spheroid and determined its principal radii by measuring radii of curvature from its side-view and front-view images acquired in situ on the tribometer setup (Fig. 3D).

In order to measure the principal radii of elytra or tergites, side-view and front-view images of the samples on the tribometer setup were captured (GigE Color Industrial Camera DFK 33GR0134, The Imaging Source, Charlotte, NC). A sketch of a representative side-view image taken from a *Stenolophus comma* elytron sample, as well as annotations that explain the measurement, are shown in Fig. 3D. The 2 mm diameter glass rod on the tribometer tip was at similar distance from the camera lens, so it was used to mark scale. The dashed ellipse drawn on the figure shows that the side-view of the elytron describes a portion of the elliptical side-view of the whole beetle body; similarly, the front-view image (not shown) shows a portion of circular front-view of the beetle body. The radii of curvature were determined from the images using an algorithm to detect the boundaries of the elytra/tergites in the image, convert them to points in coordinate system, and then fit circles onto the points using Pratt's method [20]. The maximum local radius of curvature at the contacting point, $\boldsymbol{R_{max}}$, was calculated from measurements of $\boldsymbol{R_x}$ and $\boldsymbol{R_y}$ from the images as per Eq. (2).

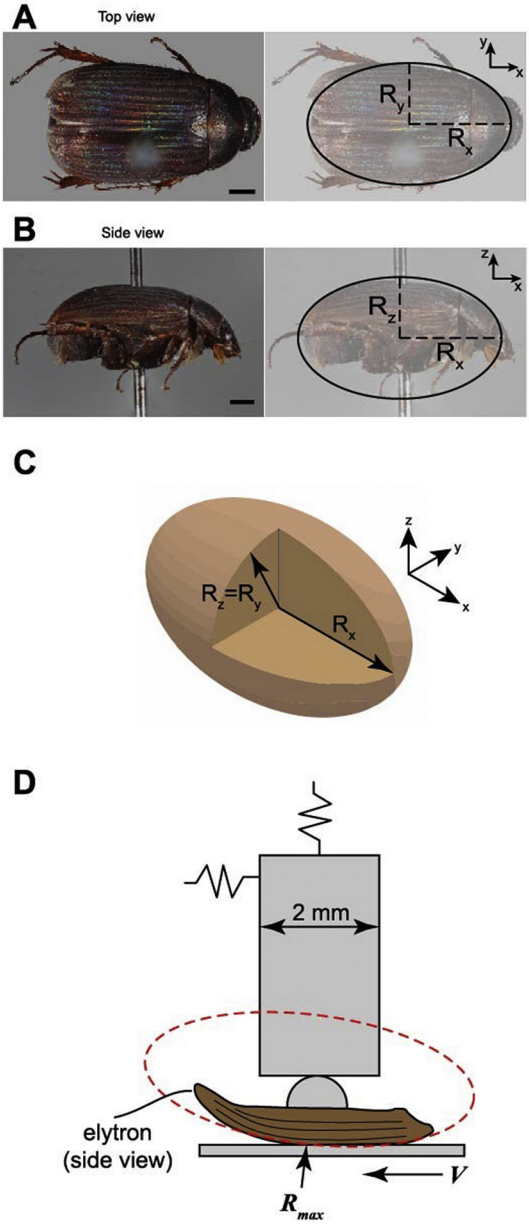

Fig. 3. The elytra and tergites of the beetles studied are curved. (A) and (B) show the top and side view of a *Serica sericea* individual. To describe the curvature of a beetle, we modeled its (A) top view and (B) side view as an ellipse, and front view (not shown) as a circle. (C) The resultant 3D model is a spheroid, which has principal radii of $\boldsymbol{R_x}$, $\boldsymbol{R_y}$ and $\boldsymbol{R_z}$, where $\boldsymbol{R_y = R_z}$. The x-axis is defined as the direction along beetle body, and the *y*- and *z*-axes are directions transverse to the body. The principal radii ($\boldsymbol{R_x}$ and $\boldsymbol{R_y}$) are different across different beetle species and quantify the extent of curvature of their body surfaces. (D) Since the elytra/tergites are surface sections of the whole beetles, the principal radii could also be determined by measuring the curvature of elytra/tergites. A representative side-view of a *Stenolophus comma* elytron sample was taken from the experimental setup when the disk was moving at a linear speed $\boldsymbol{V}$, and was used to determine the principal radii. Principal radius transverse to the beetle body ($\boldsymbol{R_y}$) was determined from the radius of curvature in front-view image (not shown). Longitudinal principal radius ($\boldsymbol{R_x}$) was determined from measuring maximum radii of curvature ($\boldsymbol{R_{max}}$) in side-view image according to Eq. (2).

$$R_{\max} = \frac{R_x^2}{R_y} \tag{2}$$

2.5. Contact Angle Goniometry

The advancing and receding contact angles (CAs) of the beetle elytra or tergites were measured as a metric of wettability (KYOWA MCA-3 microgoniometer, Kyowa Interface Science Co. Ltd. and FAMAS InterFAce Measurement & Analysis System). Three droplets were placed in a line along the anterior-posterior axis on the elytra or tergites of each individual ($N = 3$ per species) of *Serica*, *Selenophorus*, *Stenolophus*, and *Philonthus/Cafius* pairs. Six droplets were dispensed along the elytra of the *Phyllophaga* pair ($N = 3$ individuals per species). Droplets were dispensed for 60 s at 70 Hz to determine the advancing CA, resulting in droplets with diameters that ranged from 100 to 520 μm, then allowed to evaporate for 60 s to determine the receding CA, with images recorded at 1 Hz. The CAs reported in this work for advancing were chosen as the highest CA that occurred while the droplets advanced. Reported receding CAs were defined as the CA when the base of the droplet receded (droplet base diameter decreased) during evaporation. Single-factor ANOVA (Analysis of Variance) ($\alpha = 0.05$) tests were done in Microsoft Excel to determine if CA differed significantly between all beetles with diffraction gratings and those without. For individual pairs, paired *t*-test (Two-Sample Assuming Unequal Variances) with $\alpha = 0.05$ were done in Microsoft Excel and one-tailed *p*-values were determined.

3. Contact Model

3.1. Normal Loading Scenarios

When water was introduced in the contact between the cuticle samples and fibrous filter paper, additional forces inherent of water need to be considered. Most notably, the water will wet both surfaces, creating a meniscus between the contacting surfaces. The pressure inside the meniscus is lower than the atmospheric pressure outside the meniscus; this pressure difference, commonly referred to as the Laplace pressure, creates additional force that pulls the two surfaces together [21]. As this pulls the probe tip downward, it appears in the force signal as increased adhesion between the two surfaces. In addition, the thin and continuous water layer caused a buoyancy force acting upward on the transducer tip. A capacitive sensor measured the total displacement of the flexure tip. Consequently, the normal force recorded in tribological experiments is the product of normal stiffness of the flexure and the flexure tip displacement. This reflects the load applied by the flexure that opposes the sum of all contact forces applied on the tip in normal direction. This load is applied externally by the flexure to the contacting system and thus is denoted *externally applied load* (***P***). Therefore, the meniscus and buoyancy force inherently contribute to the externally applied load ***P*** in addition to the contact load between the surfaces themselves, such as they would be in the absence of a fluid. For lightly loaded sliding experiments, the effect of these forces is more significant as they are comparable to the contact load. The externally applied load ***P*** is thus equal to the sum of all contact forces in the normal direction: the contact load ***N***, the meniscus force $\boldsymbol{F_m}$, and the buoyancy force $\boldsymbol{F_b}$ (Eq. (3)) (shown schematically in Fig. 2D). Eq. (3) also means that the externally applied load ***P*** can be a negative value while the surfaces are in contact (non-zero dry load), if the summation of contact load ***N*** and buoyancy force $\boldsymbol{F_b}$ is smaller than the meniscus force $\boldsymbol{F_m}$.Combining the normal load with the coefficient of sliding friction $\boldsymbol{\mu}$ through the classical friction law gives an expanded expression for the friction force $\boldsymbol{F_F}$ (Eq. (4)). The meniscus force less the buoyancy force represents the net force due to the interaction between water and the sample surface. This quantity will be denoted the *net adhesion force* in the rest of the manuscript. The friction coefficient as a ratio of forces further means that a linear least-squares fitting of all measured friction forces versus externally applied load results in both a fit for the friction coefficient and the intercept on the friction force axis $\boldsymbol{F_{INT}}$ (Eq. (1)). For dry experiments $\boldsymbol{F_{INT}} \rightarrow 0$, though for wet experiments it is expected to be positive due to the added adhesion (Eq. (5)).

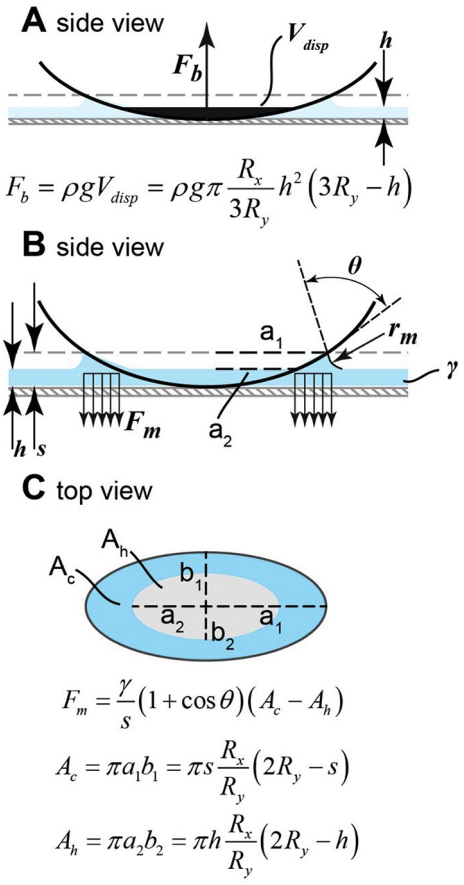

Fig. 4. (A) Buoyancy force was calculated by multiplying density of water (ρ), gravitational acceleration (***g***) and area of water displaced ($\boldsymbol{V_{disp}}$), which is equal to the volume of immersed portion of the modeled spheroid. This volume is related to the principal radii ($\boldsymbol{R_x}$ and $\boldsymbol{R_y}$) of the spheroid, as well as the water layer thickness (***h***). (B) The meniscus force is dependent on the surface tension (γ) of water and the contact angle of water (**θ**) for the elytron/tergite. The applied area of the meniscus is around the periphery of contact region, defined by the elliptical cross-cut area at average meniscus height (***s***) with a major axis of $\mathbf{2a_1}$ subtracted by projected area of submerged portion under water layer thickness (***h***) with a major axis of $\mathbf{2a_2}$. The distributed load $\boldsymbol{F_m}$ shows the location where the meniscus force is applied. Although meniscus force may not be uniformly distributed in reality, it is estimated uniform in the theoretical calculation in this manuscript (See Section 3.3). (C) The top-view schematic shows the definition of the applied area more clearly. The meniscus is applied at the light-blue area ($\boldsymbol{A_c - A_h}$). The meniscus cross-cut area ($\boldsymbol{A_c}$) is elliptical and depends on principal radii ($\boldsymbol{R_x}$ and $\boldsymbol{R_y}$) of the modeled spheroid and average meniscus height (***s***), while the submerged area ($\boldsymbol{A_h}$) depends on principal radii and water layer thickness (***h***). Real area of contact is included in the submerged area; schematic is not to scale. (color online) (For interpretation of the references to color in this figure legend, the reader is referred to the web version of this article.)

$$F_m = \iint_\Omega \Delta p(x,y)\, d\Omega = \iint_\Omega \frac{\gamma}{r_m} d\Omega \tag{9}$$

$$r_m \approx \frac{s}{\cos\theta_1 + \cos\theta_2} \tag{10}$$

$$F_m \approx \gamma(\cos\theta_1 + \cos\theta_2) \iint_\Omega \frac{1}{s} d\Omega \approx \frac{\gamma}{s}(\cos\theta_1 + \cos\theta_2)\Omega \tag{11}$$

$$P = N - F_m + F_b \tag{3}$$

$$F_F = \mu N = \mu(P + F_m - F_b) \tag{4}$$

$$F_{INT} = \mu(F_m - F_b) \tag{5}$$

3.2. Buoyancy Force

A body immersed in a liquid experiences an upward force due to the liquid pressure difference below and above the body. The magnitude of the force is a function of the mass of the displaced liquid $\rho \cdot \boldsymbol{V_{disp}}$ and the gravitational constant $\boldsymbol{g} = 9.8\,\mathrm{ms}^{-2}$ (Eq. (6)). In this study, the volume of water displaced by the elytra or tergites was the volume of the spheroid portion that is below the water layer (Fig. 4A), equivalent to the volume of the spheroidal cap cut at water layer thickness $\boldsymbol{h}$, which can be easily calculated using geometry (Eq. (7)). Inserting this volume gives an expression that can be evaluated for the theoretical buoyancy force acting in each experiment (Eq. (8)). Density is that of water: $\rho = 1000\,\mathrm{kg{\cdot}m}^{-3}$.

$$F_b = \rho g V_{disp} \tag{6}$$

$$V_{disp} = \pi h^2 \frac{R_x}{3R_y}(3R_y - h) \tag{7}$$

$$F_b = \rho g \pi \frac{R_x}{3R_y} h^2 (3R_y - h) \tag{8}$$

3.3. Meniscus Force

The meniscus force between two contacting surfaces with additional externally-applied load is related to the surface energy of the fluid γ and the radius of the meniscus $\boldsymbol{r_m}$ (Fig. 4B). The general form begins with an integration of the pressure difference between the liquid-air interface and the pressure within the liquid over the projected area of meniscus onto a flat plane Ω (Eq. (9)) [22].

If the effective section of a meniscus is approximated as an arc (which is true under negligible van der Waal and gravitation forces), the effective radius of meniscus is the ratio between meniscus height $\boldsymbol{s}$ and the sum of the cosines of the static contact angles, θ_1 and θ_2; θ_1 defines the angle between the water and paper while θ_2 defines the angle between the water and beetle sample surface (Eq. (10)) [21]. Contact angle is dependent on interfacial energy at the solid-liquid interface [23]; thus, the meniscus radius $\boldsymbol{r_m}$ is different for different solid surfaces, leading to different meniscus force. Substituting that definition of $\boldsymbol{r_m}$ results in an expression for meniscus force that is a function of the contact angles (Eq. (11)). Following the model by Tian and Bhushan, we assume that variations of the meniscus height are negligible [21].

The projected area of the meniscus is defined by subtracting the projected area of the portion submerged under the water layer, $\boldsymbol{A_h}$, from the area defined by the periphery of the meniscus, $\boldsymbol{A_c}$ (Fig. 4C). The submerged area is subtracted because the submerged portion is at atmospheric pressure, resulting in zero Laplace pressure and thus no meniscus force. The real contact area, which should also be subtracted from the projected area of meniscus [21], is included in the submerged area. These area variables were substituted into Eq. (11) to arrive at Eq. (12). The water layer thickness on the paper is about 1.25 mm, which is much larger than the mean height of surface asperities on both contacting surfaces; therefore, all asperities at the nominal contact area can be assumed as immersed in the water, so that a single, large meniscus spans the entire nominal cross-sectional area. This assumption converts the summation term to a single term. In addition, a thin water layer on the paper means that the fluid bridge spans between the fluid surface and the sample, or $\theta_1 \rightarrow 0$ [23]; the simplified expression is shown by Eq. (13). Using the geometrical description of beetle body given in Section 2.4, the areas, $\boldsymbol{A_c}$ and $\boldsymbol{A_h}$, can be calculated as the base ellipse area of spheroidal caps that are cut off at different heights. The area defined by the periphery of the meniscus, $\boldsymbol{A_c}$ is the base ellipse area of the spheroidal cap cut off at the meniscus height $\boldsymbol{s}$ (Eq. (14)); the projected area of submerged portion, $\boldsymbol{A_h}$ is that cut off at the water layer thickness $\boldsymbol{h}$ (Eq. (15)). Substituting Eqs. (14) and (15) into Eq. (13), the equation for the theoretical force is shown in Eq. (16).

$$F_m \approx \frac{\gamma}{s}(\cos\theta_1 + \cos\theta_2) \sum_i (A_c^i - A_h^i) \tag{12}$$

$$F_m \approx \frac{\gamma}{s}(1 + \cos\theta_2)(A_c - A_h) \tag{13}$$

$$A_c = \pi s \frac{R_x}{R_y}(2R_y - s) \tag{14}$$

$$A_h = \pi h \frac{R_x}{R_y}(2R_y - h) \tag{15}$$

$$F_m = \frac{\gamma \pi R_x}{sR_y}(1 + \cos\theta)[s(2R_y - s) - h(2R_y - h)] \tag{16}$$

4. Results

The surface microstructures from a single individual from each species were imaged using SEM. Experiments and measurements were conducted on three individual samples per beetle species ($N = 3$) to account for biological variability across individuals. To ensure reproducibility, tribological experiments were repeated for three trials at each sliding speed for each individual sample. Goniometry measurements were conducted on at least three different locations on each individual sample.

4.1. Microscale Surface Features

By comparing SEM images across the selected contrasting pairs, we identified two types of surface sculpturing that could both function as diffraction gratings (Fig. 5). The species studied, as well as the descriptions of their corresponding surface sculpturing, are summarized in Supplementary Table S1 according to descriptors first used by Harris [24]. The first type, observed on the iridescent species of Carabidae (*Sel. opalinus* and *St. anceps*), is characterized by highly regular grooves (substrigulate) aligned in parallel with spacing ~900 nm and groove radii ~160 nm, spanning the wavelengths of visible light. In addition, the cross-section image of *Sel. opalinus* reveals that the plateaus between the grooves are slightly inclined toward the posterior of the body. These features are absent on their non-iridescent counterparts (*Sel. ellipticus* and *St. comma*), and rather they have incomplete hexagonal structures (sculpticells), with characteristic length of about 10 μm, which is much larger than wavelength of visible light. In addition, they are flat, as shown in the cross-section image of *Sel. ellipticus*. For the pair of species of Staphylinidae, the tergite surface sculpturing is similar to that observed in Carabidae. The iridescent species (*Phi. cyanipennis*) has parallel grooves, and the non-iridescent one (*C. canescens*) has hexagonal structures. However, this pair shows significantly distinct spatial density of setae. The iridescent species has much lower setae density across the tergite than its non-iridescent counterpart. In addition, there are nanoscale grooves and ridges present on the setae of both staphylinid species. Those features have a periodicity of ~600 nm.

The second type was observed on the iridescent species of Scarabaeidae (*Ser. sericea* and *Phy. rorulenta*). Regular, hair-like protrusions with high spatial density of characteristic spacing ~760 nm likely act as diffraction gratings. The cross-section of *Ser. sericea* confirms that the protrusions have a high aspect ratio. Their non-iridescent counterparts (*Ser. campestris* and *Phy. pronunculina*) show rows of shorter, more irregular and spatially-sparse protrusions. Spacing between rows is about 3–5 μm, much larger than the wavelength of light. The cross-section image of *Ser. campestris* shows that the surface sculpturing is also flat. Generally, iridescent species have more developed and regularly aligned surface sculpturing with characteristic dimensions and spacings < 1 μm. Their non-iridescent counterparts have

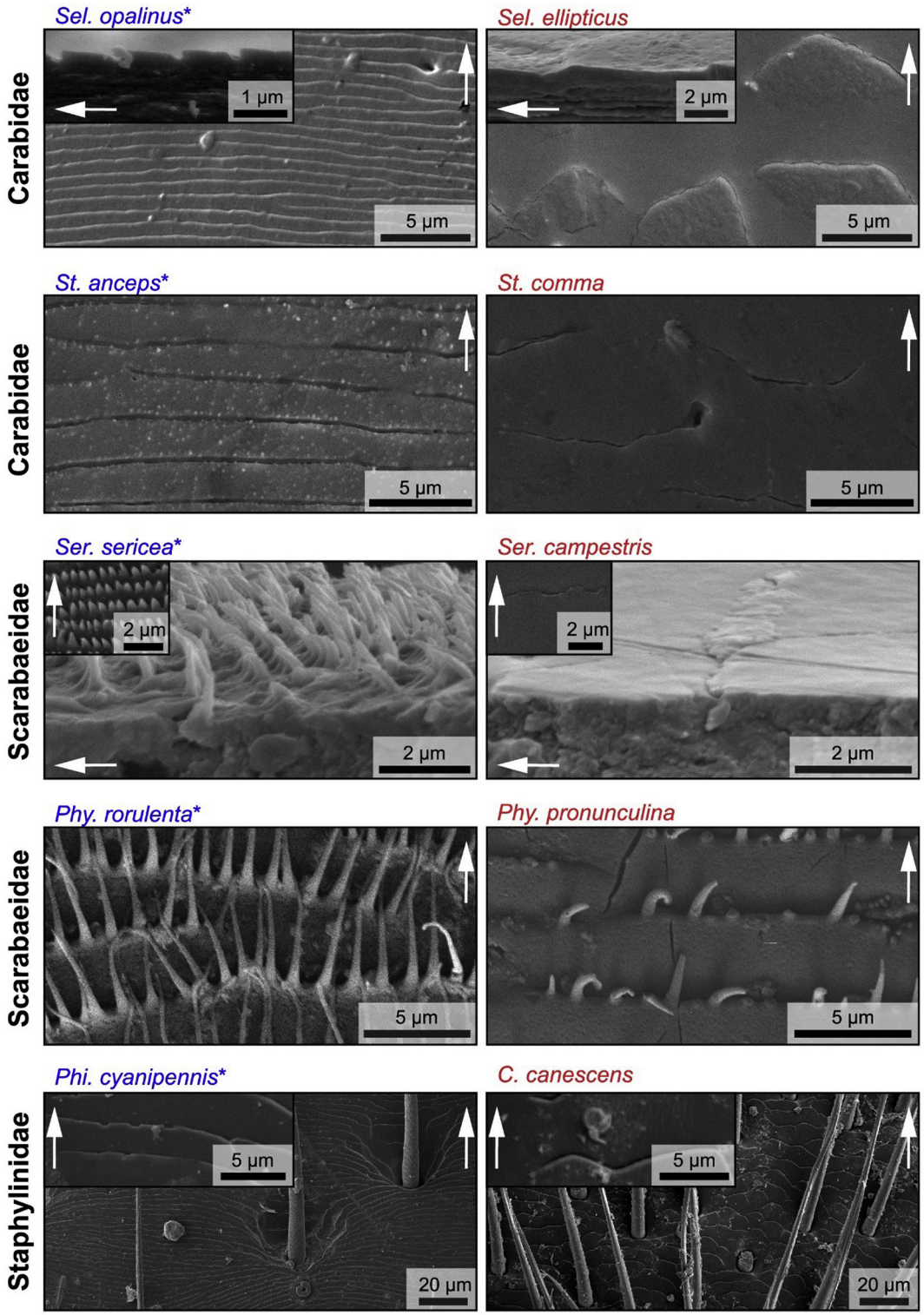

Fig. 5. Representative SEM micrographs of all beetle species studied. Images of species within the same contrasting pair are shown in the same row, along with their corresponding families. Iridescent species are shown on the left, and non-iridescent ones are shown on the right. The white arrows indicate the direction from the anterior to the posterior of beetle bodies.

less-developed, sparser features ~3–10 μm, or are missing high-aspect features completely.

4.2. Sliding Friction

Least-squares regression fits were done on each set of measured forces for each experiment: friction force $\boldsymbol{F_F}$ and externally applied load $\boldsymbol{P}$ as described in Section 3. A sample plot of the data for *Serica* spp. pair at sliding speed of $\boldsymbol{V} = 5$ mm/s is shown in Fig. 6. Representative data for every pair at sliding speed of $\boldsymbol{V} = 5$ mm/s is provided in Fig. S1; lines fit with an average of $\boldsymbol{R^2} = 0.81$. The average coefficient for the 3 experiments on different individuals is plotted in Fig. 7 versus the input sliding speed. Coefficients under both dry and wet conditions do not depend on sliding speed. For every beetle species, regardless of the

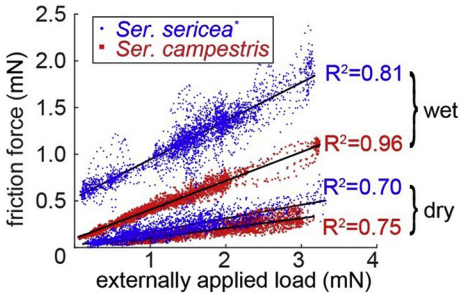

Fig. 6. Frictional force vs. externally applied load plot after smoothing, from experimental trials at $\boldsymbol{V}$ = 5 mm/s under both wet and dry conditions, for a representative Serica spp. pair. Actual datapoints after smoothing are represented by four sets of scattered points. Each set belongs to results of a species under an experimental (dry or wet) condition. Blue dots belong to the iridescent species are red squares belong to the non-iridescent species. A best-fit line determined from least-square fitting is plotted coincident with each set of data points. An R^2 value is shown next to each best-fit line. (For interpretation of the references to color in this figure legend, the reader is referred to the web version of this article.)

iridescence, the friction coefficients measured in the wet environment were significantly higher than those in dry sliding (Fig. 7 Left).

For the two pairs in the Scarabaeidae (Fig. 7B), iridescent species have dry and wet friction coefficient different from their non-iridescent counterparts, which means that the friction coefficient difference between the two species within a contrasting pair is larger than the variation between identical individuals, as calculated by the sample standard deviation. This is shown by little or no coincidence of the shaded regions between the two contrasting species. For the pairs that belong to Carabidae (Fig. 7A) and Staphylinidae (Fig. 7C), the dry and wet friction coefficients of iridescent species were similar to their non-iridescent counterpart, shown as some coincidence in the shaded regions between the two contrasting species.

The intercepts of the linear fits, $\boldsymbol{F_{INT}}$, are shown as bar plots on the right side of Fig. 7. The intercepts under dry sliding are much smaller compared to those under wet sliding for all species expect *St. anceps* and *St. comma*, where both dry and wet intercepts are close to zero. This matches with the modeling of normal loading scenario under dry and wet conditions (Section 3.1).

4.3. Sample Geometry

Following the general shapes observed in Fig. 3, the radii determined by photography reveal larger dimensions in the plane longitudinal (axial) to the body, $\boldsymbol{R_x}$, and smaller dimensions in the plane transverse to the beetle body, $\boldsymbol{R_y}$, summarized in Table S2. A sample species with moderate size would have a longitudinal dimension $\boldsymbol{R_x}$ of 4.40 mm, and a transverse dimension $\boldsymbol{R_y}$ of 1.79 mm. In other words, the beetles are longer than they are wide, and the sliding experiments are oriented along the length axial to the body. Notably, the iridescent species of each contrasting pair generally had larger elytra or tergite radii, especially for the longitudinal radius. Using Eqs. (7) and (14), the meniscus cross-sectional area $\boldsymbol{A_c}$-$\boldsymbol{A_h}$and water displacement volume $\boldsymbol{V_{disp}}$ were calculated along with estimated water layer thickness of $\boldsymbol{h}$ = 1.25 mm and average meniscus height of $\boldsymbol{s}$ = 1.5 mm.

4.4. Surface Wettability

Average advancing and receding contact angles for all species studied are shown in Fig. 8. No overarching trend of differences between iridescent and non-iridescent species was found (advancing: P = .729, F = 0.121, df = 1; receding: P = .893, F = 0.018, df = 1). However, within different families, some trends were observed. For the two pairs within Scarabaeidae (Fig. 8B), the iridescent species have both higher

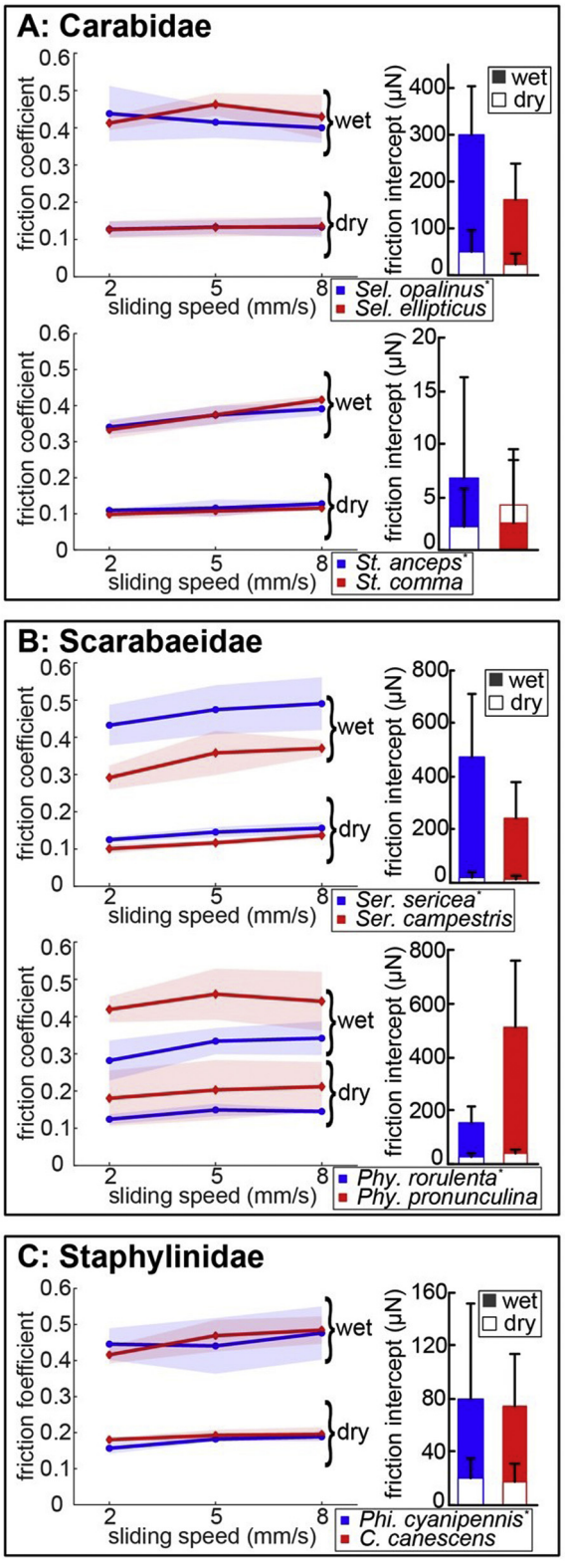

(caption on next page)

advancing and receding CAs than their counterparts (*Serica* spp. pair advancing: P = .008, t = 2.716, df = 16, receding: P = .043, t = 1.834, df = 16; *Phyllophaga* spp. pair advancing: P = .029, t = 1.981, df = 28, receding: P = .013, t = 2.332, df = 30). Within each pair, the iridescent species has both CAs significantly larger than its counterpart (P < .05). This means that for the two scarabaeid pairs, the iridescent species are more hydrophobic than their counterparts. For the two pairs

Fig. 7. Friction experiment results for all species that belong to (A) Carabidae, (B) Scarabaeidae and (C) Staphylinidae. Results for different contrasting pairs are shown in different plots. Each friction coefficient plot shows average friction coefficients across three individuals, each with three experimental trials, plotted against their corresponding sliding speeds. The dots represent average values and shaded regions represent sample standard deviations. The experimental condition is indicated in braces. Each friction intercept plot shows average measured friction intercepts. Error bars represent sample standard deviation. For all plots, the results of iridescent species are shown in blue, and the results of their non-iridescent counterparts are shown in red. (For interpretation of the references to color in this figure legend, the reader is referred to the web version of this article.)

within Carabidae (Fig. 8A), both advancing and receding CAs of iridescent species are smaller than their counterparts; however, the differences of both advancing and receding CAs between iridescent species and their counterparts were not significant (*Selenophorus* spp. pair advancing: $P = .176$, $t = -0.965$, $df = 13$, receding: $P = .181$, $t = -0.943$, $df = 13$; *Stenolophus* spp. pair advancing: $P = .247$, $t = -0.711$, $df = 10$, receding: $P = .213$, $t = -0.827$, $df = 11$). For the pair within Staphylinidae (Fig. 8C), the iridescent species has significantly smaller CAs (more hydrophilic) than its counterpart (advancing: $P = .004$, $t = -3.125$, $df = 13$, receding: $P = .001$, $t = -3.933$, $df = 11$).

4.5. Model Fit

The forces that describe the contact model are the same forces expected to give rise to friction in the sliding experiments. Thus, a comparison between the model and the sliding experiments is focused on the adhesion experienced during the sliding in the wet condition. Specifically, the *net adhesion force* was compared. From the experimental data, the net adhesion force $\boldsymbol{F_m}$-$\boldsymbol{F_b}$ was calculated by re-arranging Eq. (5), and the values were determined by the ratio of the two fitted parameters, $\boldsymbol{F_{INT}}$ and $\boldsymbol{\mu}$ (Eq. (17)). From the model, the net adhesion force is the difference of the derived expressions for $\boldsymbol{F_b}$ (Eq. (8)) and $\boldsymbol{F_m}$ (Eq. (16)). The full expression is shown in Eq. (18). The model expression requires various constants in addition to the principal radii measurements $\boldsymbol{R_x}$ and $\boldsymbol{R_y}$ (Table S2), and static CA $\boldsymbol{\theta}$ (Fig. 8): water surface tension of $\gamma = 72$ mN/m, water layer thickness of $\boldsymbol{h} = 1.25$ mm and estimated average meniscus height of $\boldsymbol{s} = 1.5$ mm. The advancing contact angles were used for $\boldsymbol{\theta}$, because these two quantities are very similar [25].

$$F_m - F_b = \frac{F_{INT}}{\mu_{wet}} \tag{17}$$

$$F_m - F_b = \pi \frac{R_x}{R_y}\left\{\frac{\gamma}{s}(1+\cos\theta)[s(2R_y - s) - h(2R_y - h)] - \frac{\rho g h^2}{3}(3R_y - h)\right\} \tag{18}$$

For *Stenolophus* and *Philonthus/Cafius* pairs, the model prediction is in relative agreement with experimental results. For other pairs, the model prediction is smaller than the experimental finding, with the exception of *Phyllophaga rorulenta*, which the model prediction is significantly larger than the experimental result (Fig. 9). Generally, the model prediction gives acceptable agreement with experimental results for species with smaller dimensions (*Stenolophus* spp., *Phi. cyanipennis* and *C. canescens*, which has cross-sectional area $< 20\,mm^2$); for larger species, the model was less able to predict the experimental result.

5. Discussion

5.1. Relationship between Diffraction Friction and Wettability

The coefficient of friction measured under the wet condition is at least twice that of the dry condition for all species studied in this manuscript. This shows that the layer of water present between the contacting interface of elytra/tergites and filter paper did not effectively reduce the friction coefficient, that is to say, water was not an effective lubricant for this contact. The contact between an elytron or tergite and laboratory filter paper was characterized by the wettability of the two surfaces. The goniometry measurements showed that the elytral/tergite surfaces were generally hydrophobic (advancing CA 70–120°); the filter paper surfaces, although not measured in goniometry, were expected to have very low contact angles due to their wicking ability, and thus manifest as strongly hydrophilic. Therefore, in the pin-on-disk tribological experiments carried out in this manuscript, the pin was hydrophobic and the disk was strongly hydrophilic. Previous studies about the effect water and oil lubrication on frictional properties of engineering surfaces with different wettability showed that for the tribological experiments using hydrophobic pin and hydrophilic disk, water could not effectively lubricate because the water repulsion generated by the relatively smaller layer of the pin was unable to influence the large, hydrophilic disk. Thus, the repulsive water layer could not be maintained, and the two surfaces remained largely in contact during sliding [26].

One implication of the hypothesis that the diffraction-grating structures also modify the friction performance is that the interaction with water provides the majority of the resistance to sliding. To test this implication, the friction coefficients for each species are plotted versus the measured contact angles (Fig. 10). There is no overarching correlation between the wet friction coefficients against filter paper and the contact angle difference between the elytra/tergites and paper surfaces for all the beetle species studied. Delineating this plot by family, the species of Scarabaeidae were generally more hydrophobic than those of Carabidae. The wet friction coefficients of scarabid species span a wider range ($0.30 \le \boldsymbol{\mu} \le 0.50$) than those of carabid species ($0.35 \le \boldsymbol{\mu} \le 0.45$). Staphylinid species had distinct degrees of wettability ($\theta \sim 70°$ for *Phi. cyanipennis* and $\theta \sim 105°$ for *C. canescens*), but the friction coefficients are similar, around the same value as the higher end for species of Scarabaeidae. Based on the available literature, the relationship between wettability and frictional properties of two contacting surfaces are still not fully understood, especially when it involves biological materials. A more recent study showed that for the contact between two engineering surfaces, where one is hydrophilic and the other is hydrophobic, with water as lubricant, the friction coefficient has a weak, negative dependence on the difference between the contact angles of the two contacting surfaces [27]. However, the result is not applicable to the study of frictional properties of beetle surfaces in this manuscript, not only because the predicted trend itself has some significant outliers that could potentially contradict it, but also because it does not involve any biological materials and hierarchical microstructures.

5.2. Type of Surface Sculptures Is Associated with Friction and Wettability

The difficulty in identifying general trends likely stems from the differences in specific surface features (Table S1) that give rise to the diffraction grating in the multiple, distinct beetle families studied. Within each family, similarities arise. Within Carabidae, the sculpturing features on the two iridescent species (*Sel. opalinus* and *St. anceps* in Fig. 5) that likely act as diffraction gratings are parallel grooves (substrigulate), whereas the features on the two non-iridescent species (*Sel. ellipticus* and *St. comma*) are hexagonal units (sculpticells). Friction coefficient results of both pairs of species (Fig. 7A) showed that the diffraction gratings do not provide significant modification of friction coefficients under both dry and wet conditions, in comparison to their non-iridescent counterparts. Goniometry measurements (Fig. 8A) showed similar results. Although both iridescent species had slightly smaller advancing and receding contact angles than their non-iridescent counterparts, the differences were not significant. This could be

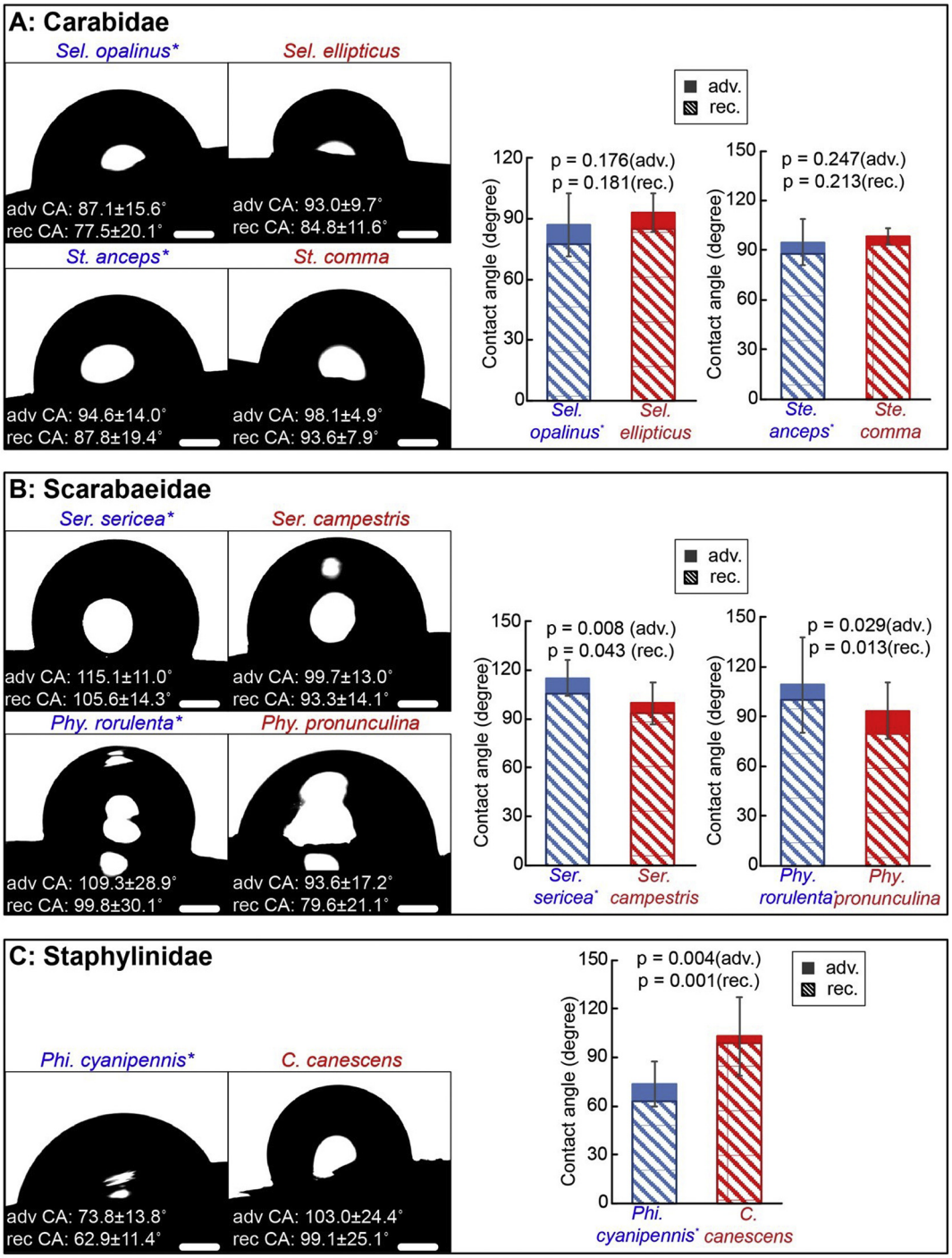

Fig. 8. Summarized results from goniometry for all species that belong to (A) Carabidae, (B) Scarabaeidae and (C) Staphylinidae. Results that belong to different contrasting pairs are shown in different plots. Left figures: show representative water droplet images that reflects average contact angles of each species. Respective advancing and receding contact angle values that are averaged across three individuals and along at least three different locations on each individual are shown in the bottom of the figures. Uncertainties represent sample standard deviations. The scale bars are all 100 μm. CA, adv and rec are abbreviations of contact angle, advancing and receding, respectively. Right figures: graphical representations of contact angle results. Filled bars represent advancing, and shaded bars represent receding contact angles. Respective *P* values determined from ANOVA tests are shown at the top of each plot.

explained by the cross-sectional topography of *Sel. opalinus* and *Sel. ellipticus* (Fig. 5): although the plateaus between the grooves on *Sel. opalinus* are inclined, they do not provide additional surface roughness. The real contact area during sliding for both iridescent and non-iridescent species within Carabidae could thus be similar, leading to similar friction coefficients. The contact angles, which are also dependent on roughness [28], were also similar for these two pairs.

On the other hand, the two iridescent species within Scarabaeidae show completely different surface sculpturing features (*Ser. sericea* and *Phy. rorulenta*), which are rows of small protrusions with high aspect ratio; their non-iridescent counterparts (*Ser. campestris* and *Phy. pronunculina*) have underdeveloped protrusions with low aspect ratio. The friction coefficient results between iridescent/non-iridescent pairs instead showed significant differences under both dry and wet conditions (Fig. 7B); similarly, these two iridescent species show significantly more hydrophobic wettability properties (Fig. 8B) than their non-iridescent

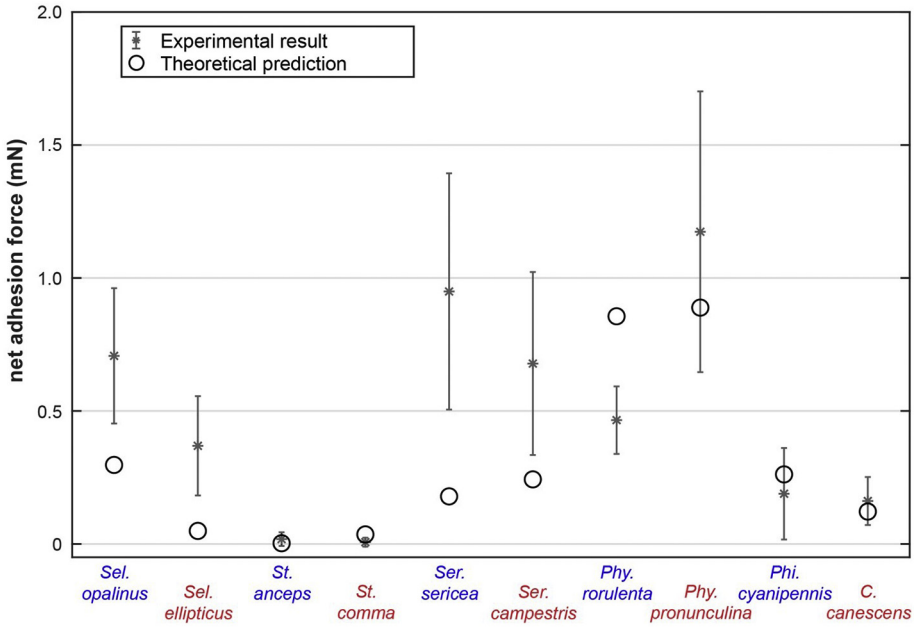

Fig. 9. Comparison between experimentally measured average net adhesion force ($F_m - F_b$) and model prediction. Error bars on experimental results are sample standard deviations across three individuals per species. The experimental result is determined from tribological experiment data using Eq. (17), and the model calculation was determined using Eq. (18). Generally, the net adhesion force on beetles of smaller size were accurately predicted by the model, but the adhesion force on larger species was underestimated by the model.

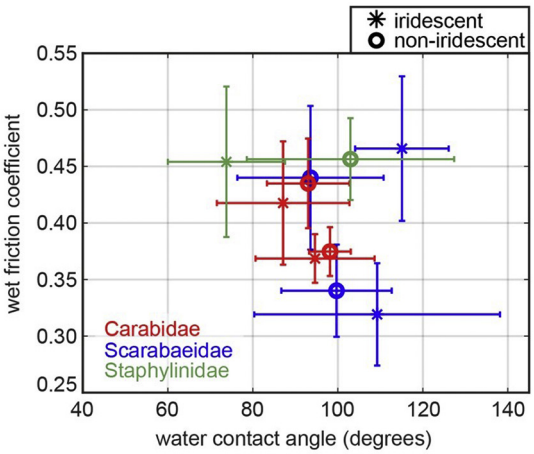

Fig. 10. Plot of friction coefficients against wet paper for all species studied, versus their corresponding average static (advancing) contact angles. Species that belong to different families are represented by different colors. Iridescent species are represented by asterisks, and non-iridescent ones are represented by filled circles.

counterparts. The high aspect ratio of protrusions on *Ser. sericea* from cross-sectional images (Fig. 5) likely reduce the real contact area between the elytron and the countersurface to be limited to the tips of the protrusions, while the *Ser. campestris* surface is mostly flat. The difference of contact area due to roughness is expected to significantly alter the friction, especially when water dynamically pins and de-pins from features as they slip against each other [29].

The pair of species within Staphylinidae, *Phi. cyanipennis* and *C. canescens* has similar surface sculpturing features as the two Carabidae pairs (Fig. 5). Although the friction coefficients (Fig. 7C) of these two species under both dry and wet conditions were similar, while the goniometry results (Fig. 8C) showed that the iridescent species were much more hydrophilic than their non-iridescent counterparts; this is the opposite trend to species of Carabidae. The iridescence was present on the tergites of the staphylinid species rather than the elytra, so potentially the anatomy of those two surfaces differed enough to account for observed differences. The dimensions and cuticle stiffness or composition may be different between them. A more likely reason is the high density of setae, or hair-like protrusions on the tergites of staphylinid species. The setae, which provide more compliance to the surface under applied loads, also could present distinct friction and wettability compared to abdominal cuticle. Previous studies on the wettability of setae showed that the setae of several insect species can be hydrophobic. The setae on legs of cranefly (*Nephrotoma australasiae*), with nanogrooves and nanoridges, and have contact angle of water > 170° [30], demonstrating superhydrophobic properties. Since the setae in the two Staphylinidae species also have nanoscale grooves and ridges, they are expected to be significantly hydrophobic, and would possibly present distinct frictional properties from cuticles as well. Therefore, isolating the staphylinid species to investigate the contributions of the setae versus cuticle to the wettability and friction response is a recommended future direction.

5.3. Model Prediction of Net Adhesion Force

In this work we aim to also analytically connect the wettability and friction performance of the beetle cuticle by modeling the forces which act at the interface. It is generally understood that hydrophobic surfaces are less wettable; however, another key factor is the magnitude of surface area pushed into contact with water. According to Eq. (15), a more hydrophobic species may experience larger meniscus forces than a less hydrophobic one, if the former has significantly larger principal radii dimensions than the latter. When taking the buoyancy force into account, it makes the scenario more complicated, and therefore we superimposed these effects to arrive at a model which captures their competition. The model is able to predict the net adhesion force within the same order of magnitude, shown in Fig. 9. Compared to the average roughness of filter paper under dry and wet conditions (< 10 μm) as well as microfeature heights on sample elytra and tergites (several hundred nanometers), the estimated meniscus height (1.5 mm) is > 150× larger. This makes the model assumptions appropriate. The net adhesion force predicted from model is smaller than that determined from tribological experiments for species with sizes relatively large (cross-sectional area > 20 mm^2). This is likely because we did not consider fluid effect due to pressure and shear stress acting on the surface of the specimen as it slides while partially immersed in water. The water flow around the specimen provides opposing force in addition to frictional force in the lateral direction, and thus would directly add to friction intercept F_{INT} determined from the fitting of

experimental data. As a result, the net adhesion force interpreted from experimental data using Eq. (17) is increased because the fluid effect influence is not separated from $\boldsymbol{F_{INT}}$. For species of larger dimensions, the fluid effect would be stronger as they have larger area subject to water flow during sliding, leading to more significant discrepancy between model prediction and experimentally determined net adhesion force. Other reason for this discrepancy could be because of misalignment in the tribometer setup, leading to nonuniform wetting of the filter paper and therefore non-constant values of $\boldsymbol{h}$ and $\boldsymbol{s}$.

Comparing the measured net adhesion force within each contrasting pair, most iridescent species experience similar net adhesion force as their non-iridescent counterparts (Fig. 9), although they have larger dimensions (Table S2). For the pair of *Phyllophaga* spp., the iridescent one has much smaller net adhesion force. This would be due to the change of their hydrophobicity compared to their non-iridescent counterparts. The presence of diffraction gratings, especially on scarabaeid species, could lead to significantly more hydrophobic body surfaces; therefore, they are able to experience less force due to water that opposes their motion while having larger body sizes.

5.4. Limitations and Recommended Directions

This work uncovers the alterations in friction correlated to surface structures, which can now be further explored as part of the larger aim of examining the adaptive role of diffraction gratings in burrowing animals. This manuscript introduces and affirms the multifunctional aspects of exoskeletal surfaces of beetles, specifically the connection between their surface microsculptures which produce iridescence, and how they control the wettability and friction response when slid against fibrous surfaces. While this study was unable to uncover overarching general trends for all species pairs, it does cover five pairs of carefully-selected species over three families, with family-dependent trends. Beetle species possessing diffraction gratings number in the hundreds, with more being discovered all the time [9], and as such future studies on specific microsculpture features (Fig. 5), isolated families, or with larger cohorts would expand on the findings in the present work.

Secondly, all tests and measurements were performed on the original, untreated beetle surfaces. This preserves any differences in chemical and material composition of the cuticle between species. Future work is recommended on species that not only resemble each other in microsculpture morphology, but also the stiffness and physiological architecture within the cuticle; this would provide more uniform samples from which to draw more subtle relationships. Coatings or surface treatments with known properties could also achieve this to some extent. Finally, this manuscript only studies frictional behavior of the beetle surfaces against fibrous surfaces represented by laboratory filter paper. Beetles encounter a number of environmental surfaces and structures, including leaf litter, rocks, sand, decaying matter, and fungus, at all states of hydration (Fig. 1) [4–6,31]. Future works need to address the extent to which other types of surfaces drive friction.

6. Conclusions

Coefficients of friction were higher by at least two times for all beetle species when their exterior elytra or abdominal tergites slid against a wetted fibrous countersurface than against a dry fibrous surface. The coefficients did not depend on sliding speed. Friction coefficients only differed between iridescent and non-iridescent species of scarab beetles.

For species of Carabidae, the surface sculpturing patterns on iridescent elytra are parallel grooves; those on non-iridescent elytra are cellular hexagons. This type of surface sculpturing on iridescent species does not elicit varying tribological and wettability properties compared to their non-iridescent counterparts.

For species of Scarabaeidae, the surface sculpturing patterns on iridescent elytra are rows of small protrusions; those on non-iridescent elytra are flatter and irregular protrusions. This type of surface sculpturing makes the elytra of iridescent species significantly more hydrophobic and have significantly distinguished friction coefficients, compared to their non-iridescent counterparts.

The species of Staphylinidae do not follow the above trend. Their surface sculpturing patterns are similar to species of Carabidae, but the iridescent staphilinid species is much more hydrophilic. There is no varying friction coefficient for the two species in the Staphylinidae contrasting pair.

The measurement of principal radii of the species studied, following the spheroid modeling, shows that all species are more curved in the direction transverse to the body. In addition, the iridescent species generally have larger dimensions than their non-iridescent counterparts.

When sliding in a wet condition, the interaction between the surfaces and water causes a friction force intercept during the fitting process that determines friction coefficient. The theoretical calculation combining meniscus force and buoyancy force is able to predict the friction force intercept accurately for some species, while underestimating others.

Acknowledgments

LW acknowledges partial support by the Campus Research Board, University of Illinois at Urbana-Champaign (UIUC). KR received generous support through the UIUC Entomology Department's Entomology Summer Stipend Award (2017 & 2019). Scanning electron microscopy was done at the UIUC Beckman Institute for Advanced Science and Technology's Microscopy Suite. Contact angle goniometry was done in the UIUC Energy Transport Research Lab led by Dr. Nenad Miljkovic. All authors are grateful for inspiration and helpful conversations with Dr. Ainsley Seago (Department of Primary Studies, Government of New South Wales, Australia). Fig. 1 was drawn by Olivia F. Boyd, Oregon State University.

Declaration of competing interests

None.

Appendix A. Supplementary data

Supplementary data to this article can be found online at https://doi.org/10.1016/j.biotri.2019.100108.

References

[1] A.E. Seago, P. Brady, J.P. Vigneron, T.D. Schultz, Gold bugs and beyond: a review of iridescence and structural colour mechanisms in beetles (Coleoptera), J. R. Soc. Interface 6 (2009), https://doi.org/10.1098/rsif.2008.0354.focus.
[2] T.F. Anderson, A.G. Richards, An electron microscope study of some structural colors of insects, J. Appl. Phys. 13 (1942) 748–758, https://doi.org/10.1063/1.1714827.
[3] E.G. Loewen, E. Popov, Diffraction Gratings and Applications, CRC Press, 1997.
[4] R.H. Arnett, M.C. Thomas, P.E. Skelley, H. Frank, American Beetles Volume 2: Polyphaga: Scarabaeoidea through Curculionoidea, (2002), https://doi.org/10.1201/9781420041231.
[5] R.H. Arnett, M.C. Thomas, American Beetles. Volumen 1. Archostemata, Myxophaga, Adephaga, Polyphaga: Staphyliniformia, (2001).
[6] C.H, Hoffmann, The Life History of *Serica Sericea* (Ill.) (Scarabaeidae-Coleoptera), 1936.
[7] H.E. Hinton, D.F. Gibbs, An electron microscope study of the diffraction gratings of some carabid beetles, J. Insect Physiol. 15 (1969) 959–962, https://doi.org/10.1016/0022-1910(69)90136-x.
[8] H.E. Hinton, D.F. Gibbs, Diffraction gratings in gyrinid beetles, J. Insect Physiol. 17 (1971), https://doi.org/10.1016/0022-1910(71)90006-0.
[9] A. Seago, Unpublished database, personal communication (2017).
[10] D. Shpeley, W. Hunting, G.E. Ball, A taxonomic review of the selenophori group (Coleoptera, carabidae, harpalini) in the west indies, with descriptions of new species and notes about classification and biogeography, Zookeys. 690 (2017) 1–195.
[11] L.W. Saylor, Synoptic revision of the testaceipennis group of the beetle genus

phyllophaga, J. Wash. Acad. Sci. 33 (1943) 106–110.
[12] M.R. Chani-Posse, A.J. Brunke, S. Chatzimanolis, H. Schillhammer, A. Solodovnikov, Phylogeny of the hyper-diverse rove beetle subtribe Philonthina with implications for classification of the tribe Staphylinini (Coleoptera: Staphylinidae), Cladistics. 34 (2018) 1–40, https://doi.org/10.1111/cla.12188.
[13] N.J. Severs, Freeze-fracture electron microscopy, Nat. Protoc. 2 (2007) 547–576, https://doi.org/10.1038/nprot.2007.55.
[14] C.A. Schneider, W.S. Rasband, K.W. Eliceiri, NIH image to ImageJ: 25 years of image analysis, Nat. Methods 9 (2012) 671–675, https://doi.org/10.1038/nmeth.2089.
[15] A.A. Pitenis, J.M. Urueña, K.D. Schulze, R.M. Nixon, A.C. Dunn, B.A. Krick, W.G. Sawyer, T.E. Angelini, Polymer fluctuation lubrication in hydrogel gemini interfaces, Soft Matter 10 (2014) 8955–8962, https://doi.org/10.1039/c4sm01728e.
[16] M. Knapp, Preservative fluid and storage conditions alter body mass estimation in a terrestrial insect, Entomol. Exp. Appl. 143 (2012) 185–190, https://doi.org/10.1111/j.1570-7458.2012.01247.x.
[17] N.E. Rank, D.A. Bruce, D.M. McMillan, C. Barclay, E.P. Dahlhoff, Phosphoglucose isomerase genotype affects running speed and heat shock protein expression after exposure to extreme temperatures in a montane willow beetle, J. Exp. Biol. 210 (2007) 750–764, https://doi.org/10.1242/jeb.02695.
[18] C.P. Wheater, Effect of starvation on locomotor activity in some predacious coleoptera (Carabidae, Staphylinidae), Coleopt. Bull. 45 (1991) 371–378.
[19] I. Hutchings, P. Shipway, Areal measures, Tribology, 2nd Editio, Butterworth-Heinemann, 2017, pp. 7–35.
[20] V. Pratt, Direct Least-Squares Fitting of Algebraic Surfaces, (1987).
[21] X. Tian, B. Bhushan, The micro-meniscus effect of a thin liquid film on the static friction of rough surface contact, J. Phys. D. Appl. Phys. 29 (1996) 163–178, https://doi.org/10.1088/0022-3727/29/1/026.
[22] H. Liu, G. Cao, Effectiveness of the young-Laplace equation at nanoscale, Sci. Rep. 6 (2016) 1–10 (doi:10.1038/srep23936).
[23] G. Whyman, E. Bormashenko, T. Stein, The rigorous derivation of Young, Cassie-Baxter and Wenzel equations and the analysis of the contact angle hysteresis phenomenon, Chem. Phys. Lett. 450 (2008) 355–359, https://doi.org/10.1016/j.cplett.2007.11.033.
[24] R.A. Harris, A glossary of surface sculpturing, Occas. Pap. Entomol. 28 (1979) 1–31.
[25] D.Y. Kwok, A.W. Neumann, Contact angle interpretation: re-evaluation of existing contact angle data, Colloids Surfaces A Physicochem. Eng. Asp. 161 (2000) 49–62, https://doi.org/10.1016/S0927-7757(99)00324-6.
[26] A. Borruto, G. Crivellone, F. Marani, Influence of surface wettability on friction and wear tests, Wear. 222 (1998) 57–65 (doi:10.1063/1.1728375).
[27] Z. Pawlak, W. Urbaniak, A. Oloyede, The relationship between friction and wettability in aqueous environment, Wear. 271 (2011) 1745–1749, https://doi.org/10.1016/j.wear.2010.12.084.
[28] Y.C. Jung, B. Bhushan, Contact angle, adhesion and friction properties of micro-and nanopatterned polymers for superhydrophobicity, Nanotechnology. 17 (2006) 4970–4980, https://doi.org/10.1088/0957-4484/17/19/033.
[29] Y. Mo, K.T. Turner, I. Szlufarska, Friction laws at the nanoscale, Nature. 457 (2009) 1116–1119, https://doi.org/10.1038/nature07748.
[30] H.-M.S. Hu, G.S. Watson, B.W. Cribb, J.A. Watson, Non-wetting wings and legs of the cranefly aided by fine structures of the cuticle, J. Exp. Biol. (2011), https://doi.org/10.1242/jeb.051128.
[31] D.D. Mckenna, A.L. Wild, K. Kanda, C.L. Bellamy, R.G. Beutel, M.S. Caterino, C.W. Farnum, D.C. Hawks, M.A. Ivie, M.L. Jameson, R.A.B. Leschen, A.E. Marvaldi, J.V. Mchugh, A.F. Newton, J.A. Robertson, M.K. Thayer, M.F. Whiting, J.F. Lawrence, A. Ślipiński, D.R. Maddison, B.D. Farrell, The beetle tree of life reveals that Coleoptera survived end-Permian mass extinction to diversify during the Cretaceous terrestrial revolution, Syst. Entomol. 40 (2015) 835–880, https://doi.org/10.1111/syen.12132.